Journal of Hydrology 624 (2023) 129924

Contents lists available at ScienceDirect

Journal of Hydrology

journal homepage: www.elsevier.com/locate/jhydrol

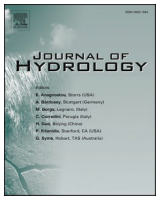

Research papers

Spatiotemporal characteristics and forecasting of short-term meteorological drought in China

Qi Zhang, Chiyuan Miao *, Jiaojiao Gou, Haiyan Zheng

State Key Laboratory of Earth Surface Processes and Resource Ecology, Faculty of Geographical Science, Beijing Normal University, Beijing 100875, China

ARTICLE INFO

Keywords:
Drought forecasting
SPEI
ConvLSTM
Flash drought
China

ABSTRACT

Intense short-term meteorological drought may lead to rapid declines in soil moisture, triggering flash drought that can cause major agricultural or socioeconomic damage. Machine learning methods have proven effective in forecasting hydrometeorology, but short-term drought forecasting is still inadequate. We developed a pentad-time-scale (5-day) standardized precipitation evapotranspiration index (SPEI-5d) to quantify short-term meteorological drought and analyzed its spatiotemporal distribution characteristics in China during the period 1962–2018. We used historical SPEI-5d as input and employed five machine learning methods for drought hindcasting: an autoregressive integrated moving average (ARIMA), random forest (RF), recurrent neural network (RNN), long short-term memory (LSTM), and convolutional long short-term memory (ConvLSTM). The results show the following: (1) During the period 1962–2018, 61.9% of the study region showed decreasing trends in drought severity, while 69.6% of the region showed increasing trends in drought intensity. (2) Drought duration, severity, and intensity have distinct seasonal characteristics, and different forecasting models perform differently in each season, with generally lower forecasting accuracy in summer and higher forecasting accuracy in winter. (3) The ConvLSTM model can capture spatiotemporal information well compared to traditional time-series forecasting models; it has the best performance (root mean square error = 0.29, and Nash-Sutcliffe efficiency = 0.92) in the test set and has high forecasting accuracy ($R^2 > 0.8$) for lead times of 1–5 days (with accuracy decreasing as lead time increases). Our findings highlight the spatiotemporal variability of short-term meteorological drought and provide valuable scientific insights for short-term meteorological drought forecasting at 1–5 days of lead time.

1. Introduction

Drought is an extreme phenomenon caused by the imbalance of water supply and demand (Jiao et al., 2021; Lesk et al., 2021), and in the context of global climate change, extreme climate events such as drought are becoming more frequent (Chiang et al., 2021). According to the Food and Agriculture Organization of the United Nations (FAO), droughts cause an average of US$250–300 billion in economic losses per year, and the frequency and magnitude of these losses will continue to increase (Xu et al., 2021a). Drought formation and evolution processes are very complex due to the participation of multiple drivers, involving meteorology, hydrology, and subsurface composition, making it hard to accurately and promptly identify drought and to plan coping strategies and preventive measures (Buttafuoco et al., 2015).

Droughts are usually classified into four types: namely, meteorological drought, hydrological drought, agricultural drought, and socioeconomic drought (Mishra and Singh, 2010). The evolution of drought involves a complex process of precipitation deficit, where meteorological drought arises due to anomalous meteorological conditions of insufficient precipitation and expanding evaporative demand, leading to the depletion of soil moisture and then eventually developing into an agricultural and hydrological drought (Xu et al., 2021b; Miao et al., 2022). Extreme climate phenomena have become more frequent in recent years due to global warming (Paprotny et al., 2018; Thirumalai et al., 2017; Zhao, 2020), and flash drought (a critical sub-seasonal phenomenon; Qing et al., 2022; Jong et al., 2022) has received increasing attention as drought research has rapidly developed. Unlike slowly developing droughts, flash drought is characterized by a sudden intensification within one or a few weeks and can quickly cause devastating socioeconomic impacts (Mukherjee and Mishra, 2022). In recent years, flash droughts have caused substantial damage worldwide (Christian et al., 2021), and they are more unpredictable than traditional

* Corresponding author.
E-mail address: miaocy@vip.sina.com (C. Miao).

https://doi.org/10.1016/j.jhydrol.2023.129924

Available online 18 July 2023

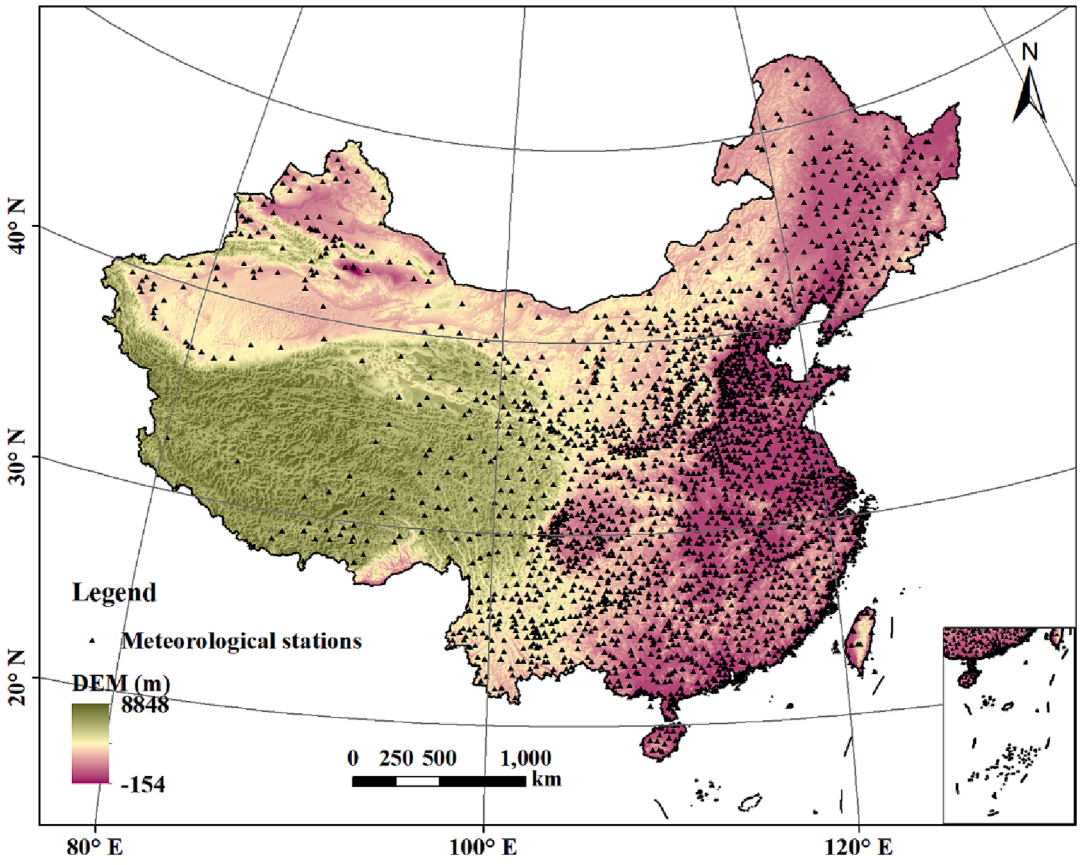

Fig. 1. Distribution of 2,419 meteorological stations in mainland China.

droughts due to their rapid development. Flash drought is usually assessed based on soil moisture (Wang and Yuan, 2021; Zhang et al., 2021), mostly on a pentad scale (5 days; Yuan et al., 2019; Gong et al., 2022). After a period of time (referred to as *propagation time*; Warter et al., 2021), meteorological drought effects may lead to a rapid decline in soil moisture and develop into a flash drought, but the recent studies focused on short-term meteorological drought seems to be insufficient.

Drought indices are commonly used to assess and monitor the spatiotemporal distribution characteristics of drought (Zhang et al., 2022a). The standardized precipitation index (SPI; McKee et al., 1993) and the standardized precipitation evapotranspiration index (SPEI; Vicente-Serrano et al., 2010) have been commonly used as meteorological drought indices. SPEI takes into account the effect of potential evapotranspiration on the basis of SPI and has different characteristics at a different temporal scales; for example, a 12-month SPEI is usually used to characterize interannual variation (Schreiner-McGraw and Ajami, 2021), the 6-month scale can measure drought in the crop growing season (April to September; Potop et al., 2014), and the 3-month scale is mostly used to describe the seasonal variation of drought (Xu et al., 2021). Since meteorological drought occurs earlier than other types of droughts, quantitative analysis and forecasting of meteorological droughts can help reduce the economic losses caused by agricultural or hydrological droughts. An increasing number of studies in recent years have focused on monitoring and forecasting of short-term drought, including flash drought (Fundel et al., 2013; Hosseini-Moghari and Araghinejad, 2015). Yuan et al. (2019) suggested that under sunny and less cloudy weather conditions, strong solar radiation increases the potential evapotranspiration capacity and even causes an increase in actual evapotranspiration at the beginning of a drought, resulting in a rapid decrease in soil moisture and thus triggering the occurrence of flash drought. Wang et al. (2021) developed the daily-scale SPEI, which can be more sensitive to monitoring daily changes compared to the conventional SPEI. Any index of short-term meteorological drought should account for both rapid intensification (i.e., the flash; Otkin et al. 2018) and drought conditions that will persist for a period of time (Gou et al., 2022). Forecasting short-term meteorological drought can help to provide early warnings and prevent the detrimental effects of flash drought.

Drought forecasting has a pivotal role in providing early warning of drought, which is intended to mitigate drought effects that could cause agricultural loss (Alawsi et al., 2022; Fung et al., 2020; Yuan et al., 2017); for example, Liang and Yuan (2021) identified the importance of initial soil moisture in forecasting flash drought by incorporating the global Weather Research and Forecasting model. Hao et al. (2018) reviewed some of the commonly used drought forecasting methods, including data-driven models (Xu et al., 2020), regression models (Sun et al., 2012), conditional probability models (Hao et al., 2016), machine learning algorithms (Xu et al., 2022), and others, each of which has advantages and disadvantages. For example, among the data-driven models, the autoregressive integrated moving average (ARIMA) model has better performance in long-term drought forecasting (Belayneh et al., 2014), but it has poor performance in capturing nonlinear features (Kim et al., 2022; Wang, 2022). Machine learning is now an important part of data-driven research in the earth sciences (Ham et al., 2019; Reichstein et al., 2019) involving the atmosphere (Retsch et al., 2022; Shen et al., 2018), land surface (Liu et al., 2022; Zhang et al., 2022b; Zheng et al., 2022), and oceans (Asgarimehr et al., 2022; Chen et al., 2019), and it has evolved rapidly over the past decade. In particular, developments in meteorology (such as random forest [RF] models) are widely used and address many problems in earth sciences and remote sensing (Gislason et al., 2006). These machine learning forecasting methods are usually divided into two main categories: time-series forecasting models and spatiotemporal forecasting models (Park et al., 2020). Artificial neural networks (ANNs) were widely adopted for time-

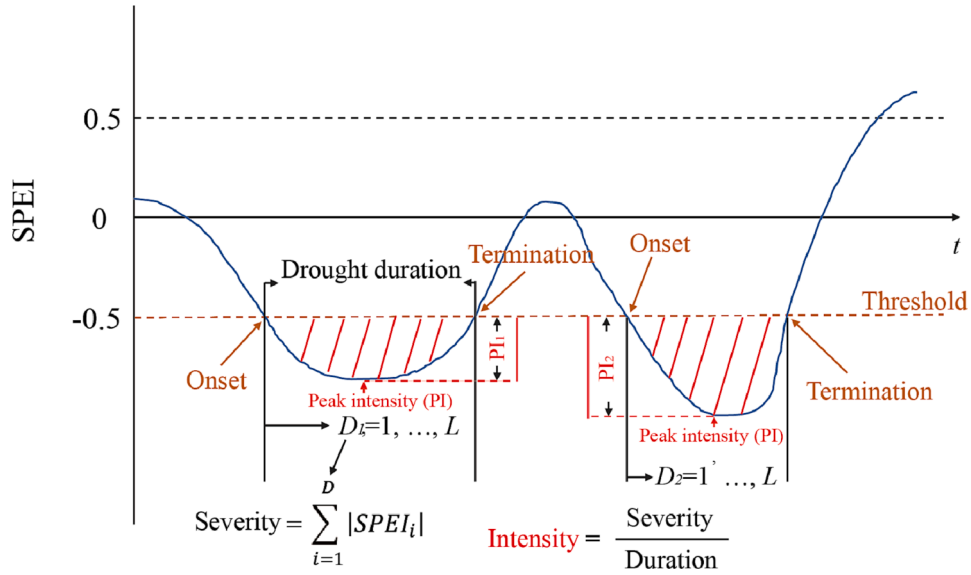

Fig. 2. Schematic diagram demonstrating the identification of drought duration, drought severity, and drought intensity from the SPEI time series. D_i and I_i, respectively, are drought duration and drought intensity for drought event $i(i = 1, 2, \cdots, L)$.

series forecasting and can capture the nonlinear information from data, but due to the large number of parameters in the training process and the long training time, they are starting to be replaced by other nonlinear models, such as recurrent neural network (RNN) models (used for short-term-memory-based tasks, insensitive to older data; Le et al., 2017). To enable long-term forecasting, RNN models were used as a basis to develop the long short-term memory (LSTM) model, which can be understood simply as a kind of RNN with more complex neurons (Dikshit et al., 2021). However, traditional time-series forecasting methods have difficulty dealing with relationships among spatially related data, because they are usually based on time series of point data as inputs. Convolutional neural network (CNN) models can extract picture features and use convolutional kernels to consider the relationships of nearby elements compared to traditional time-series models (Krizhevsky et al., 2017; Oquab et al., 2014). Ham et al. (2019) used transfer learning to train a CNN model to forecast the latitudinal distribution of sea surface temperature and found that the weaknesses of the dynamic forecasting model were overcome and satisfactory results were achieved. The coupling of CNN and LSTM models (i.e., convolutional long short-term memory; ConvLSTM) proposed by Shi et al. (2015) can capture both temporal and spatial features of the data; this model is prominent in precipitation nowcasting but is seldom applied in short-term meteorological drought forecasting.

In recent years, despite the frequent occurrence of flash drought, existing studies have mainly focused on drought forecasting at long time scales, while analysis and forecasting at short time scales have not received as much attention, and spatial relations and connections among data are usually neglected in the forecasting methods. Therefore, we calculated a pentad-scale (5-day) SPEI (SPEI-5d) to characterize the cumulative impact of short-term meteorological drought, and we compared the use of ARIMA, RF, RNN, LSTM, and ConvLSTM models to forecast SPEI-5d. This paper aims to address the following questions: (1) What are the spatiotemporal distribution characteristics of short-term meteorological drought in China? (2) Which model is most suitable for forecasting short-term meteorological drought? (3) What are the differences in the spatiotemporal characteristics and forecasting effects of short-term meteorological drought for each season?

2. Material and methods

2.1. Data and drought index

Observed daily data were acquired from the China Meteorological Administration (https://data.cma.cn/) for precipitation, maximum temperature, mean temperature, minimum temperature, wind speed, and sunshine duration from 1962 to 2018 at 2,419 meteorological stations (Fig. 1) in mainland China.

We used the pentad scale (5 days) as the minimum time unit and calculated SPEI values by sliding forward one day at a time (Wang et al., 2021a), and the resulting SPEI values are represented by SPEI-5d. For the calculation of potential evapotranspiration, we used the Penman-Monteith methods (Allen et al., 1998). According to recommendations from the literature (Stagge et al., 2015; Wang et al., 2021a), the calculation of SPEI assumes a generalized extreme value (GEV) distribution. The detailed calculation formula can be found in the supplementary material, and drought classification is shown in Table S1.

2.2. Drought definition and characteristics

We computed the drought duration, severity, and intensity to describe and analyze drought characteristics (Bevacqua et al., 2021). We set the threshold value to −0.5 (Wu and Chen, 2019), and an SPEI value below the threshold value is the beginning of the drought event, while SPEI returning to or exceeding the threshold represents the end of the drought event. Drought duration is defined as the length of time SPEI is continuously below the threshold, drought severity refers to the sum of the absolute values of SPEI during drought events, and drought intensity is the ratio of drought severity to drought duration (Fig. 2):

$$\text{Drought duration} = t_n - t_p \quad (1)$$

$$\text{Drought severity} = \sum_{t_p}^{t_n} |SPEI| \quad (2)$$

$$\text{Drought intensity} = \frac{\text{Drought severity}}{\text{Drought duration}} \quad (3)$$

where t_n and t_p represent the end and beginning of a drought event, respectively.

In addition, we used the Mann-Kendall trend test (M-K) method (Wu et al., 2018) to test for monotonic trends in time series; this test is widely

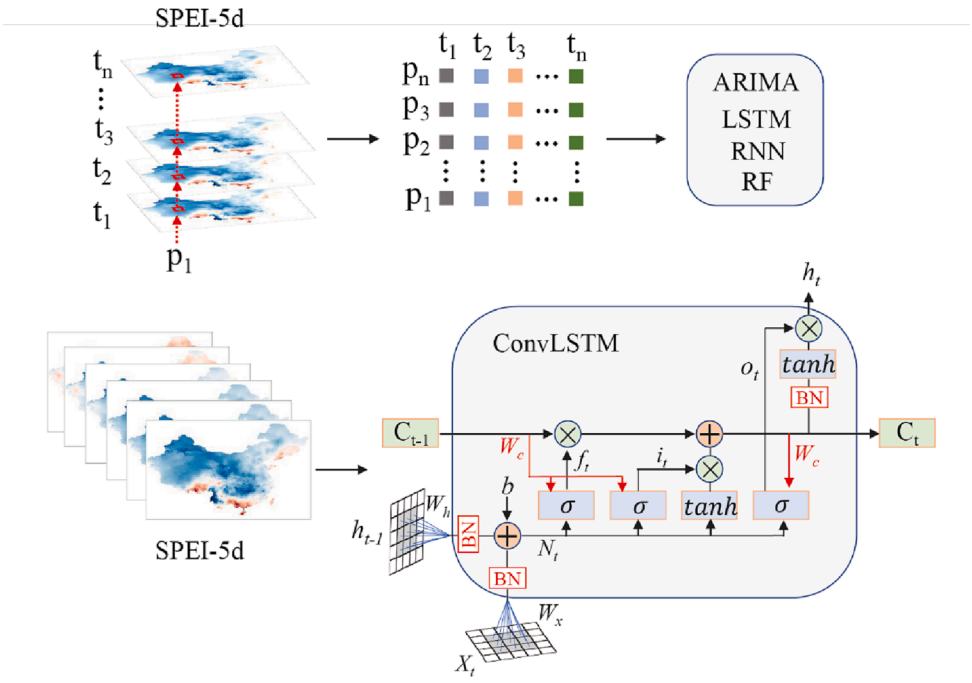

Fig. 3. The structure of a convolutional long short-term memory (ConvLSTM) network and processing workflow for the training of forecasting models (ARIMA, LSTM, RNN, RF, and ConvLSTM). Here, X_t, C_t, and h_t refer to the input, internal, and external states, respectively, at time t. W_x and W_h are the weight matrixes for the variable N_t. BN represents the batch normalization operation. σ and *tanh* are sigmoid and hyperbolic tangent activation functions, respectively. The variables f_t, i_t, and o_t represent the forget gate, input gate, and output, respectively. The elementwise multiplication of two vectors is denoted by $\otimes$ and addition by and b is the corresponding biases.

used in hydrometeorology, and the Z-value in the M-K test is usually used to determine whether the trend is consistently increasing or decreasing. We calculated the mean values of drought duration, drought severity, and drought intensity for each year from 1962 to 2018 and used M-K to obtain the annual trends. Trend significance was tested at the $\alpha = 0.05$ ($1.96 \leq |Z| < 2.58$) significance level. Positive values of the Z statistic indicate upward trends over the whole time series, whereas negative values of the Z statistic indicate downward trends over the whole time series. If a drought event spanned a natural year, we counted the event as belonging to the earlier year; for example, for the last drought event at the end of 2000 that extended into 2001, we counted it as a drought event for the year 2000.

2.3. Forecasting models

We used historical SPEI-5d data as input for the five models. The time span from 1962 to 2018 was divided into a training period (1962–2007), a testing period (2008–2017), and a one-year hindcast (2018) period, and the calculated SPEI-5d values from the periods 1962–2007 and 1962–2017 were used as input data in the model to forecast the SPEI-5d in the testing period (2008–2017) and hindcast period (2018), respectively. The data were entered using two formats for model training (Fig. 3): (1) by traversing each pixel of the training set and inputting the data into the time-series forecasting models (ARIMA, RF, RNN, and LSTM); and (2) by inputting each image into the spatiotemporal forecasting model (ConvLSTM). The early stopping method was used in this study to prevent overfitting (Xu et al., 2022). Given the model's requirement for a complete time series as input, we evaluated the forecasting performance of the SPEI-5d series, which comprises both wet (SPEI > 0) and dry (SPEI < 0) components. However, to analyze drought-related factors such as duration, severity, and intensity, we restricted our analysis to the time series that met the criteria for dry conditions (SPEI < 0), as detailed in Section 2.2. In addition, we looked at the performance of the models in each month and each season of the test period; For example, when evaluating January, we chose the average of all the January months of the test period. And for the seasons, we defined winter as December–February, spring as March–May, summer as June–August, and autumn as September–November.

2.3.1. Autoregressive integrated moving average (ARIMA) model

The commonly used methods for stochastic time-series analysis are divided into two categories: stationary time series and non-stationary time series. The autoregressive moving average model, ARMA(p,q), is composed of an AR(p) model and an MA(q) model for stationary time-series model forecasting from Box and Jenkins (1976). In contrast, non-stationary time series need to be modeled for forecasting by adding a d-difference step to ARMA(p,q) to form an ARIMA(p,d,q) model. The detailed calculation formula can be found in the supplementary material. ARIMA modeling usually consists of the following four steps:

(1) Generating time series: We took the SPEI-5d from 1962 to 2018 in China as input and traversed each pixel element to generate multiple time-series data sets.
(2) Stability testing: Since the ARIMA(p,d,q) model is a stationary time series ARMA(p,q) model obtained by d differencing, the stationarity of the time series should be judged before modeling, and we used the augmented Dickey-Fuller test (ADF) to determine the stationarity.
(3) Model determination: The autocorrelation function (ACF) and partial autocorrelation function (PACF) were used to determine the order for the ARMA(p,q) model (Fig. S1), while in the actual operation, since the program automatically traverses all pixels, the Akaike information criterion (AIC) and Bayesian information criterion (BIC) were used to automatically determine the order of the optimal model ARMA(p,q).
(4) Model testing: The ARIMA model was tested by examining the independence of the residual series. We combined Q-Q plots (Fig. S1) and the normal distribution to test whether the residuals of the model were normally distributed with a mean of zero and constant variance, then we combined this information with the Ljung-Box test (Xu et al., 2020) to determine whether the model residuals were white noise.

2.3.2. Random forest (RF) model

A random forest (RF) is a supervised learning algorithm that constructs multiple decision trees called forests and combines them for more accurate and stable forecasting (Feng et al., 2019; Gislason et al., 2006). The RF model mainly consists of two parts: a subset of training samples

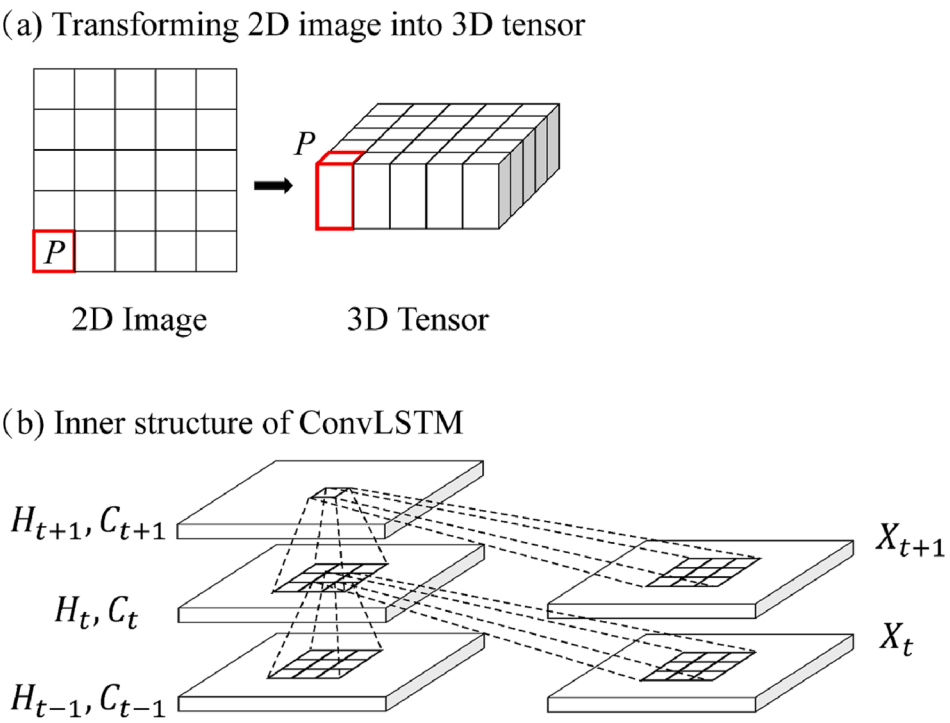

Fig. 4. Input data structure and internal structure of the ConvLSTM model. Figure adapted from Shi et al. (2015).

and a sub-category model. The training sample subsets are obtained from the original training set by simple random sampling (bootstrap random sampling), and the sub-category model is generally a decision tree algorithm. Based on *M* sets of training samples, *M* sub-forecast models can be constructed; based on each sub-forecast model, a corresponding forecast result can be obtained, and then *M* forecast values can be obtained. RFs can be used for classification as well as for regression. The main difficulty is in the selection of decision tree types, because specific classes of decision trees are chosen according to the specific task. For a classification problem, a test sample is sent to each decision tree for prediction and is then voted on, and the class with the most votes is the final classification result. For a regression problem, the forecasting result of the random forest is the mean of all decision tree outputs.

2.3.3. Recurrent neural network (RNN) model

Traditional neural networks do not take into account the effect of information from the previous moment on the current moment in forecasting analysis, while RNNs can capture time series well and take into account the effect of the previous moment on the current moment due to their special self-looping structure (Le et al., 2017). An RNN is divided into an input layer, a hidden layer, and an output layer, where a recurrent network structure is added to the hidden layer as a memory unit and neuron nodes are interconnected. Therefore, the hidden layer neurons receive not only the output information of the neurons in the previous layer but also the output information of the neurons in this layer from the previous time step, forming a network structure with loops, which stores the information of each time step and transfers sequence information. The RNN structure and detailed formulas are shown in the supplementary material.

2.3.4. Long short-term memory (LSTM) model

The special feature of an LSTM compared with an RNN is that the structure of its hidden layer is more complex, and a cell state gate structure is added to control the flow of memory information to achieve long-term transmission and memory of information (Yang et al., 2019). Therefore, an LSTM model is more suitable than an RNN to deal with sequences with longer time information and can carry the information of longer time steps (Cui et al., 2022). In this study, the LSTM model has a chain structure similar to an RNN (Fig. S2) after unfolding, and the structure diagram of an LSTM model unfolded by time dimension is shown in Fig. S3. The core and cellular unit of the LSTM model are essentially different from those of an RNN. To handle control of the model information, three gate structures are constructed in the LSTM model: an input gate, forgetting gate, and output gate. The essence of the gate structure is a fully connected layer with a built-in activation function to filter the information and let the current information pass selectively. The input is a feature vector, and the output is a probability value with a value range of [0, 1]. The details of the LSTM structure (including hidden layer; Fig. S4) and formulas are shown in the supplementary material.

2.3.5. Convolutional long short-term memory (ConvLSTM) model

The ConvLSTM model is one of the learning models specifically designed for spatiotemporal sequences and is a combination of CNN and LSTM models. Shi et al. (2015) changed the computation of the internal state and state transfer of neurons from a matrix multiplication operation to a convolutional computation, enabling the ConvLSTM model to capture not only temporal correlations but also spatial features like a convolutional layer.

The input structure of the model is shown in Fig. 4a. It is assumed that the network of *M***N* constitutes a dynamic system in the specific spatial region, and *M, N* denotes the number of rows and columns of lattice points, respectively. Each SPEI-5d map contains not only the numerical values but also the physical characteristics of the pixel at the current moment, while *P* denotes the scale of each pixel (i.e., the dimension of the physical quantity). The information observed at each time point can be considered to be a *P***M***N* tensor, denoted by *X*, and the sequence in a period of observation time is denoted by $\{X_1, X_2, \cdots, X_n\}$. The spatiotemporal sequence forecasting uses the sequence composed of the first *J* tensor to forecast the sequence composed of the next *K* tensors with the following equation:

$$\widetilde{X}_{t+1}, \cdots, \widetilde{X}_{t+K} = \arg\max_{X_{t+1}, \cdots, X_{t+K}} p(X_{t+1}, \cdots, X_{t+K} | \widehat{X}_{t-J+1}, \widehat{X}_{t-J+2}, \cdots, \widehat{X}_t) \quad (4)$$

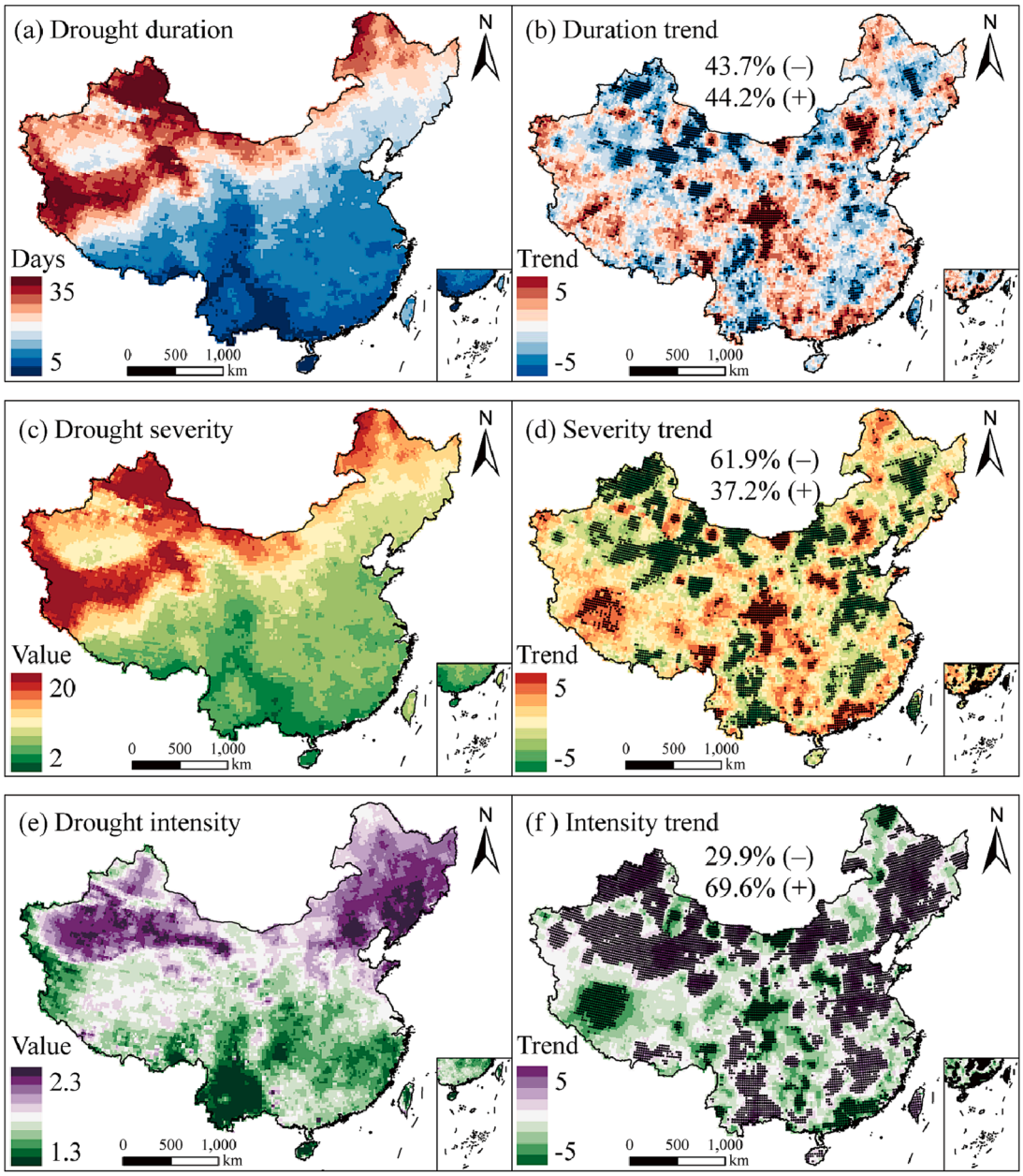

Fig. 5. (a, c, and e) Annual average drought duration, severity, and intensity from 1962 to 2018 in China. (b, d, and f) Annual average drought duration, severity, and intensity spatial trends from 1962 to 2018 in China; black dots are locations that pass the significance test (α = 0.05); "(+)" indicates the percentage of area with increasing trends and "(–)" indicates the percentage of area with decreasing trends.

Similar to the LSTM, the ConvLSTM model uses a gate unit to control the current input, which can be seen as a fusion of convolution and LSTM. The internal structure of the single-layer ConvLSTM is shown in Fig. 4b. The inputs X, C (cell output), and H (the hidden layer) are three-dimensional data, and the dashed lines in Fig. 4b indicate the use of convolution operations to pass the inputs X, C, and H from the previous moment.

The internal gate unit of ConvLSTM is connected in the same way as in LSTM, although LSTM uses a fully connected approach, while ConvLSTM uses a convolutional approach to extract features. The external structure of the ConvLSTM is shown in Fig. 3 and uses the following equations:

$$i_t = \sigma(W_{xi} * X_t + W_{hi} * H_{t-1} + W_{ci} \circ C_{t-1} + b_i) \quad (5)$$

$$f_t = \sigma(W_{xf} * X + W_{hf} * H_{t-1} + W_{cf} \circ C_{t-1} + b_f) \quad (6)$$

$$C_t = f_t \circ C_{t-1} + i_t \circ tanh(W_{xc} * X_t + W_{hc} * H_{t-1} + b_c) \quad (7)$$

$$O_t = \sigma(W_{xo} * X_t + W_{ho} * H_{t-1} + W_{co} \circ C_t + b_o) \quad (8)$$

$$H_t = O_t \circ tanh(C_t) \quad (9)$$

where σ denotes the sigmoid activation function, $\circ$ denotes the corresponding element of the matrix is multiplied, and * denotes the convolution calculation. The information is passed through the forgetting gate f_t to decide whether to continue to pass it backward. The information that continues to be passed flows into the input gate, and the information that needs to be updated is updated through the *tanh* layer. The convolution calculation is done for X_t, H_{t-1}, respectively combined with C_{t-1} to get H_t and C_t, and the result X_{t+1} is convolved to get H_{t+1} and C_{t+1}. The training phase of the ConvLSTM model uses supervised learning; the output of the network is obtained by forward propagation,

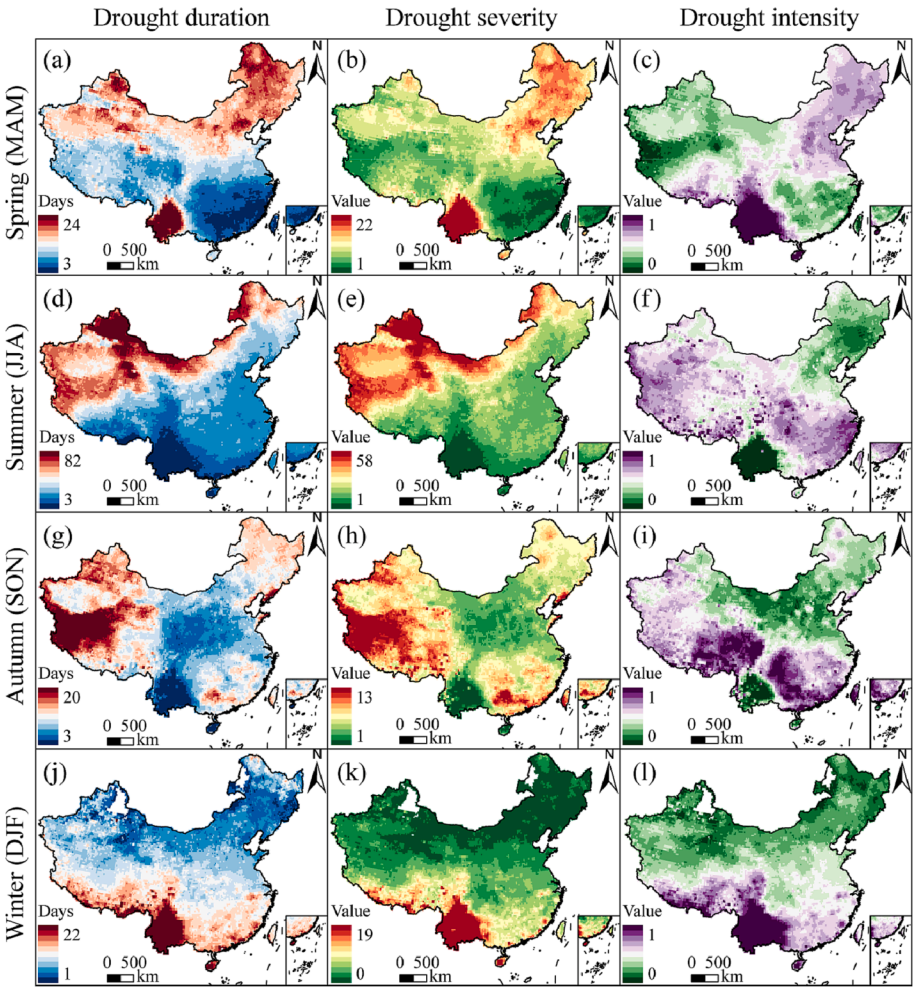

Fig. 6. Annual average drought duration, severity, and intensity from 1962 to 2018 in China for four seasons: (a, b, c) spring, (d, e, f) summer, (g, h, i) autumn, and (j, k, l) winter. Some grid points in the northwest and northeast of China are blank in winter (j, k, l) because there is no drought in these areas.

and the parameters of the network are updated by back propagation. The details and formulas of forward propagation and backward propagation of the ConvLSTM model are shown in the supplementary material.

2.3.6. Models compared

These five models are commonly used for time-series forecasting in various fields, such as meteorology and transportation. In terms of complexity, the ConvLSTM and LSTM models are more complex than RNN, ARIMA, and RF. These models share similarities in that they all require model tuning and evaluation for online learning. For example, the ARIMA model needs appropriate autoregressive and moving average selection; RF requires determination of the number of decision trees; and RNN, LSTM, and ConvLSTM require the right number of neurons. In terms of training time and model forecasting, ARIMA trains faster and works better for periodic data, while RF requires a large amount of training data to improve its accuracy. RNN, LSTM, and ConvLSTM have slower training times but provide better forecasting results for data with strong long-term dependencies.

2.4. Evaluation indices

We use Taylor diagrams (Taylor, 2001) to show the performance of the five models in the test set, which include standard deviation and correlation metrics to match observed and forecasted data. To evaluate the accuracy of the model in the test set, we used mean absolute error (MAE), mean squared error (MSE), root mean square error (RMSE), the ratio of RMSE to the standard deviation of the observations (RSR), the ratio of standard deviations (RSD), and the Nash-Sutcliffe efficiency coefficient (NSE). We used the coefficient of determination (R^2) to evaluate the accuracy of the model for spatial distribution forecasting at each lead time and MSE to evaluate the loss function of the models. Details of all evaluation indices formulas are shown in the supplementary material.

3. Results and discussion

3.1. Drought characteristics

Fig. 5 shows the trends in duration, severity, and intensity of short-term meteorological drought (SPEI-5d) in China during the period 1962–2018. We found that drought duration is longer in northern China and shorter in southern China (Fig. 5a). Similar results were found by Yu et al. (2014), who calculated drought duration based on monthly-scale SPEI values for >600 stations and found that drought duration was longest in northern, northwestern, and southwestern China during the period 1951–2010; the spatial distribution of drought duration is highly consistent with our results, although we used daily units. Fig. 5b shows that the areas with a significant increasing trend in drought duration are more extensive than those with a decreasing trend. From Fig. 5a and c, we can see that the spatial distribution of drought severity is similar to the spatial distribution of drought duration, while Fig. 5d shows that the

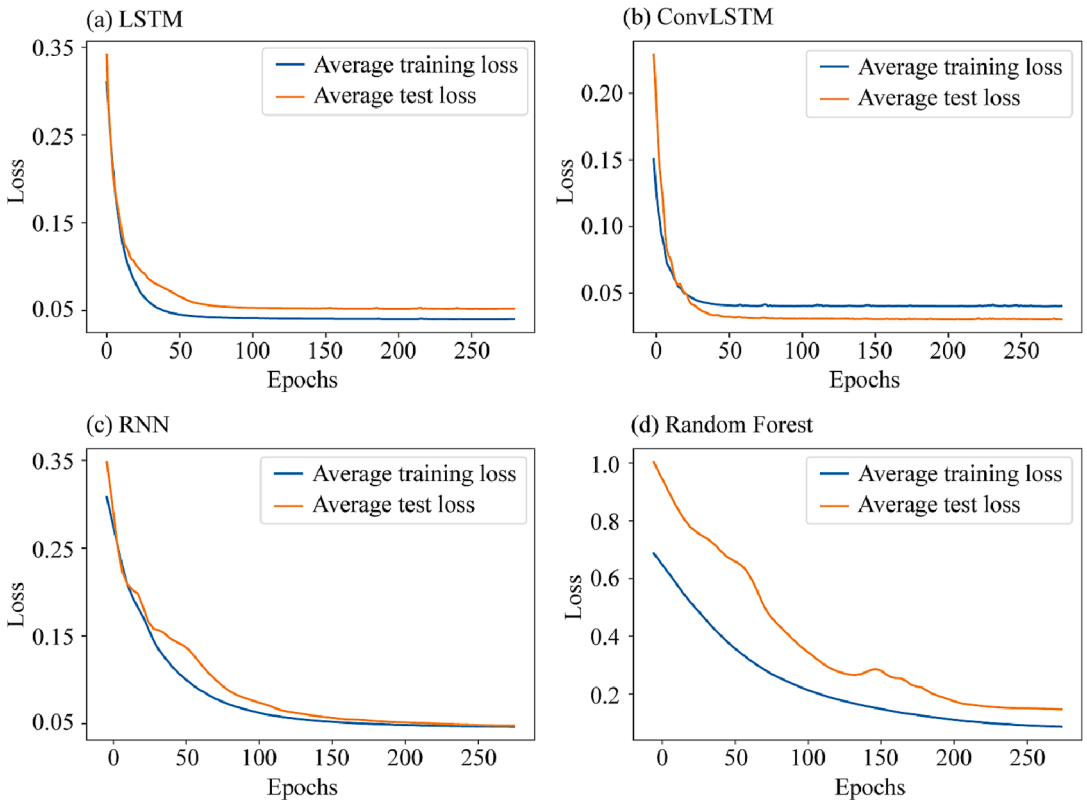

Fig. 7. Mean squared error (MSE) loss in forecasting models (LSTM, ConvLSTM, RNN, RF) for training (1962–2007) and testing sets (2008–2017).

total area where drought severity decreases is much larger than the area where it increases, especially in northwest China, where most locations show a significant decreasing trend, which is similar to the spatial distribution shown in Fig. 5b. There are indications that the decrease in drought severity in northwest China may be due to global warming and the Pacific Decadal Oscillation (PDO; Apurv et al. 2019). Fig. 5e shows that the drought intensity in northern China is higher than in southern China, especially in northwestern and northeastern China where the drought intensity is the greatest. This may be due to the long sunshine duration and high potential evapotranspiration in these areas, resulting in a high cumulative impact of meteorological drought in the short term (Li et al., 2020; Zhang et al., 2016). Fig. 5f shows that the overall area of increased drought intensity is larger than the area of decreased intensity. The distribution of areas with a significant increase in drought intensity suggests potential impacts on agriculture, such as to corn and wheat in north and northwest China and to rice in southwest China; in northwest and northeast China, especially, there was also a notable increase, suggesting that the impact of short-term meteorological drought in these regions may be greater—i.e., it may lead to a rapid decrease in soil moisture and trigger flash drought (Ford and Labosier, 2017).

The drought severity based on SPEI-5d tended to decrease in most areas during the period 1962–2018 (61.9%; Fig. 5d) while the drought intensity tended to increase in most areas (69.6%; Fig. 5f); because of this, we extracted annual meteorological elements such as precipitation, mean temperature, potential evapotranspiration, and the number of drought events for areas with significant increases and decreases in drought severity and drought intensity (Fig. S5). Using Equation (2) in Section 2.2, it is not difficult to find that drought severity is closely related to drought duration ($t_n - t_p$), and when the number of drought events is higher, the drought severity increases. As illustrated in Fig. S5c and S5e, our findings reveal that all temperatures exhibited an increasing trend despite the fact that temperatures in areas with significantly increasing drought severity were generally lower than those in areas with significantly decreasing drought severity. In contrast, there was a significant difference in PET–P between areas where severity was significantly increasing or decreasing. In particular, areas with higher PET–P values (Fig. S5e) experienced more severe aridity, indicating insufficient water availability for soil and vegetation. These conditions were mainly observed in China's arid regions, particularly in the northwest and southwest, including the deserts of Xinjiang, which receive the least precipitation. However, in northwest China since 1980, the temperature has shown a trend of increasing year by year, with a particularly notable increase in Xinjiang, while the precipitation has been increasing year by year, especially in summer and autumn, and droughts are occurring less frequently, leading to a trend of decreasing drought severity. Taking Xinjiang in northwest China as an example, drought occurs less frequently (yellow line graph in Fig. S5d and S5f) due to warming and humidification in northwest China (Yang et al., 2022). However, when the difference between potential evaporation and precipitation (PET-P) is large (Fig. S5d and S5f), drought may have a great impact on the local ecosystem, and once drought occurs, drought intensity is usually high (Fig. 2). In addition, some studies have shown that while the decrease in regional precipitation has played an important role in the pattern of drought intensity changes over the past half century (Su et al., 2018), drought intensity is more sensitive to changes in temperature (Han et al., 2021).

We also calculated the average annual drought duration, severity, and intensity for each season. Since some pixels for each season did not experience drought in a given year, the spatiotemporal data were discontinuous, and therefore we did not calculate the trends. Fig. 6 shows drought has notable differences by season. The drought duration and severity in southwest China are greater in spring and winter, while in northwest China, drought duration and severity are greater in summer and autumn. Xu et al. (2021c) found that the interannual variation of precipitation was consistent with that of SPEI for approximately 70%–80% of China, while the spring precipitation showed a significant decreasing trend in southwest China, which might be the reason for the long spring drought duration in southwest China. Fig. 6a–c shows that in

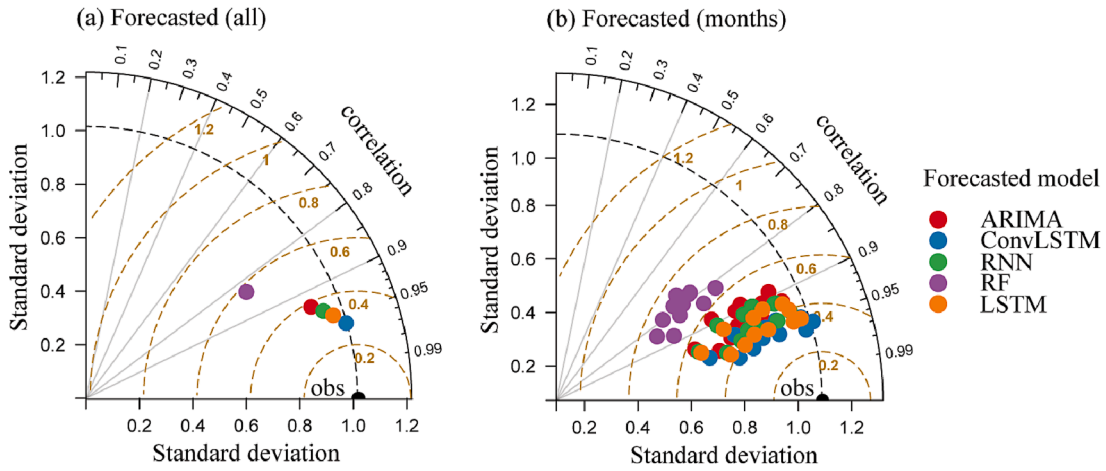

Fig. 8. Taylor diagrams displaying a statistical comparison of forecasting models (ARIMA, LSTM, RNN, RF, and ConvLSTM) in the test set (2008–2017) of (a) all SPEI-5d values (average of the sequence of all pixels from 2008 to 2017) and (b) every month of SPEI-5d values (average of the sequence of all pixels for each month from 2008 to 2017 is extracted separately).

Table 1
Performance measures for comparison of observed and forecasted SPEI-5d for different temporal periods in China (based on the average of all pixels of the test set; 2007–2017).

Temporal period	Model	MAE	MSE	RMSE	RSR	RSD	NSE
All data	ARIMA	0.29	0.16	0.40	0.40	0.89	0.84
	ConvLSTM	0.21	0.08	0.29	0.28	1.00	0.92
	RNN	0.25	0.11	0.34	0.33	0.96	0.89
	RF	0.45	0.34	0.58	0.57	0.71	0.67
	LSTM	0.26	0.13	0.35	0.35	0.93	0.88
Spring	ARIMA	0.30	0.16	0.40	0.41	0.88	0.84
	ConvLSTM	0.23	0.09	0.30	0.31	1.02	0.91
	RNN	0.27	0.13	0.36	0.37	0.98	0.86
	RF	0.49	0.37	0.61	0.61	0.69	0.62
	LSTM	0.29	0.14	0.38	0.38	0.93	0.85
Summer	ARIMA	0.34	0.23	0.48	0.46	0.90	0.79
	ConvLSTM	0.24	0.11	0.33	0.32	0.99	0.90
	RNN	0.29	0.16	0.40	0.38	0.96	0.86
	RF	0.51	0.45	0.67	0.64	0.67	0.59
	LSTM	0.31	0.17	0.42	0.40	0.92	0.84
Autumn	ARIMA	0.28	0.16	0.40	0.44	0.91	0.80
	ConvLSTM	0.18	0.07	0.27	0.30	0.99	0.91
	RNN	0.21	0.09	0.31	0.34	0.95	0.88
	RF	0.40	0.29	0.54	0.60	0.72	0.64
	LSTM	0.22	0.11	0.33	0.36	0.93	0.87
Winter	ARIMA	0.24	0.10	0.31	0.35	0.90	0.88
	ConvLSTM	0.17	0.05	0.22	0.25	0.99	0.94
	RNN	0.21	0.07	0.27	0.30	0.96	0.91
	RF	0.39	0.24	0.49	0.54	0.73	0.70
	LSTM	0.21	0.07	0.27	0.30	0.94	0.91

spring, in southwest China the drought duration, severity, and intensity are high, while the spatial patterns of drought duration and severity in northwest China are opposite. Fig. 6d–f shows a pattern of high drought duration and severity in northwest China during summer. This is because northwest China is an arid region where the potential evapotranspiration is much higher than the precipitation. Elsewhere, the intensity of summer drought was also great in the southeast, which may be due to the higher precipitation, temperature, and actual evaporation in the southeast of China in summer, resulting in a faster water cycle than in the northwest and thus a shorter drought duration and greater drought intensity in southeast than in northwest China. Fig. 6g–i shows that the drought duration and severity in autumn are greater in southeast and western China, especially in western China, where high altitude, high solar radiation intensity, and great precipitation variability are the most important factors influencing the overall impact of drought (Li et al., 2019), along with the relatively low precipitation in autumn, when higher temperatures are the main cause of warming and drying in the region. Fig. 6j–l shows that the drought duration, severity, and intensity in winter are greatest in southwest China. During winter in most parts of China, the canopy of most ecosystems is dormant and photosynthesis is minimal (Ma et al., 2019); however, Li et al. (2014) showed that actual evapotranspiration is greatest in southwest China during winter, which may be contributing to the longer drought duration. On the other hand, when the Arctic Oscillation is in the negative phase, the cold-air activity in east Asia is strong and the path is eastward, and the cold air reaching the southwest region is weak, resulting in less winter precipitation in the region and making it prone to drought (Tan et al., 2017).

3.2. Overall performance of forecasting models

We used the easily convergent MSE as the loss function for evaluating the training and testing process of the models and found that the values of the loss function for the training and testing sets of all models continuously decreased and converged, indicating that the training and testing sets were well fitted without overfitting (Fig. 7).

According to Fig. 8, the forecasting accuracy of all five models is generally high, with the ConvLSTM model having the highest prediction accuracy (NSE = 0.92), because it can capture the information of both temporal and spatial dimensions more effectively; next are LSTM (NSE = 0.88), RNN (NSE = 0.89), and ARIMA (NSE = 0.84), while RF (NSE = 0.67) has the lowest accuracy (Table 1). Among the models, the forecasting accuracy of the ARIMA, LSTM, RNN, and ConvLSTM models are close. Tian et al. (2021), who reported similar findings to ours, used RF, LSTM, and other models to forecast multi-month-scale SPEI for multiple sites and found that the LSTM model has higher accuracy compared to RF (e.g., 6-month-scale SPEI, MSE_{LSTM} = 0.3849, MSE_{RF} = 0. 4368). Akbari Asanjan et al. (2018) used LSTM and RNN to forecast short-term precipitation and found that LSTM outperformed RNN because RNN could not learn from past information, while LSTM could handle data that was more time dependent due to its special "gate" settings; their findings are similar to the conclusions of our short-term meteorological drought forecast. Xu et al. (2022), similarly, found that the LSTM model outperformed the ARIMA model at all time scales (1–12 months) when forecasting multi-scale SPEI, but for shorter time scales (1-month-scale

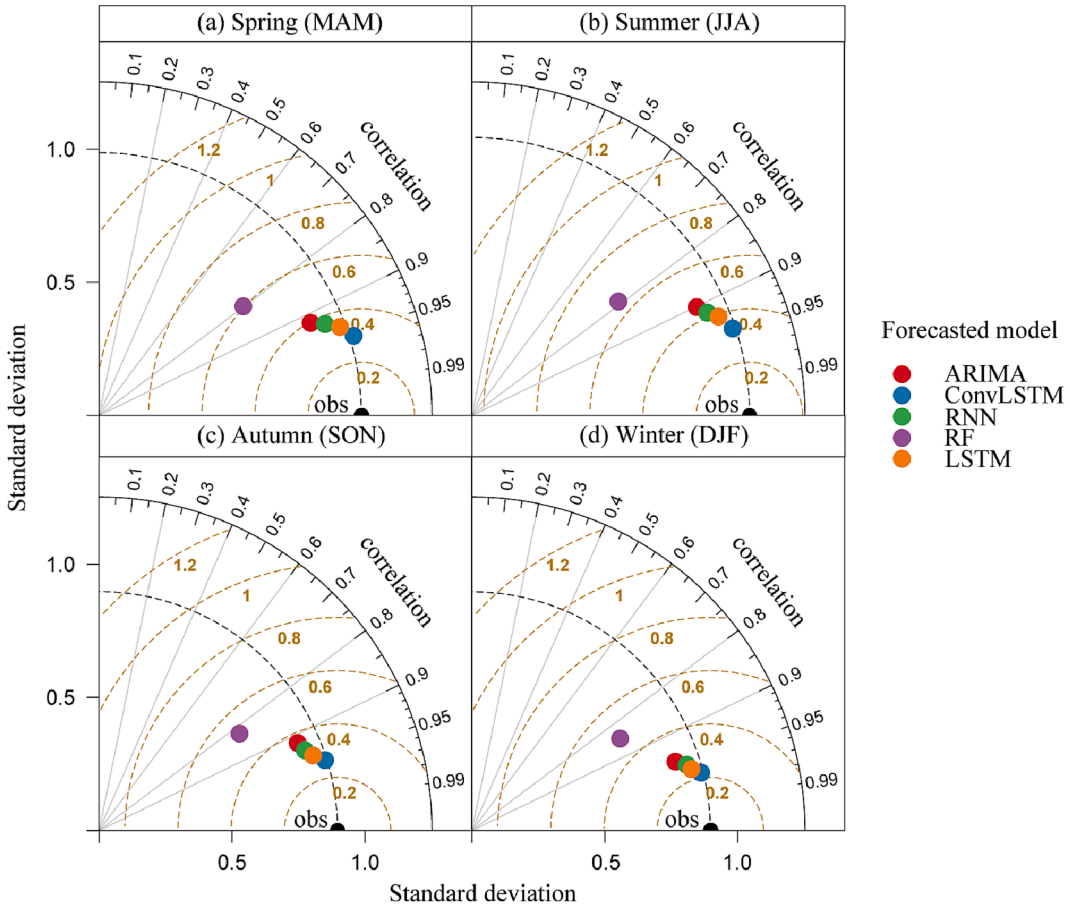

Fig. 9. Taylor diagrams displaying a statistical comparison of forecasting models (ARIMA, LSTM, RNN, RF, and ConvLSTM) in the test set (2008–2017) of SPEI-5d values for (a) spring, (b) summer, (c) autumn, (d) and winter.

SPEI), the difference in forecasting accuracy between ARIMA and LSTM was not notable; we also found that in short-term meteorological drought forecasting, there may be no obvious trend in the fluctuation of the SPEI-5d time series, resulting in the minimal differences in the forecasting accuracy of all models.

We also evaluated the performance of all models for each season. Fig. 9 shows that for each season, all models performed similarly to what we show in Fig. 8, with the ConvLSTM model having the highest accuracy, followed by LSTM, RNN, ARIMA, and finally RF. This is mainly because ConvLSTM models are spatiotemporal forecasting models; the input data uses an entire image of each time slice as input to train the model and forecasts (Ulloa et al., 2022). In contrast to traditional time-series forecasting models (RF, ARIMA, RNN, and LSTM), the ConvLSTM model considers the spatial relationships between all neighboring pixels, whereas time-series forecasting models traverse each pixel for data input, modeling, and forecasts, which ignores spatial interactions (Wang et al., 2021b). However, model performance also varies between seasons; for example, all models performed best in winter, followed by autumn and spring, while all models performed the worst in summer. This may be due to the fact that in summer, precipitation and potential evapotranspiration vary widely in the northern and southern regions of China, and the model performance is averaged over all pixel points in the country; therefore the averaged SPEI-5d series features differ greatly in the north and south of China, and it is relatively difficult for the model to capture the time-series features during model training, thus generating differences in forecasting accuracy.

According to Figs. 8 and 9, the ConvLSTM model performed best in the test set, so we also verified its accuracy for spatial distribution forecasting at each lead time. As shown in Fig. 10, the ConvLSTM model has the highest spatiotemporal forecasting accuracy ($R^2 = 0.96$) for a lead time of 1 day, but the accuracy decreases as the lead time is extended, with $R^2 = 0.85$ when the lead time is 5 days, and $R^2 = 0.66$ when the lead time is 10 days, indicating that the model can forecast the spatial distribution of SPEI-5d in the next 1–5 days with high accuracy. Li et al. (2021) also looked at forecasting with the ConvLSTM model, and they found that forecasting soil moisture had a high accuracy with 1–7 days of lead time, while Dikshit et al. (2021) reported a high accuracy with 1–6 months of lead time when using the LSTM model to forecast monthly-scale SPEI. This is similar to our results in that the forecasting accuracy is higher for 1–5 days of lead time, but the accuracy decreases as the lead time increases. We also examined the spatial forecasting performance of the ConvLSTM model for a 1-day lead time for each season; we chose the first day of the middle month of each season in 2018 for comparison purposes. As shown in Fig. 11, the spatial performance of the ConvLSTM model with a 1-day lead time for each season is good ($R^2 > 0.9$), indicating that the ConvLSTM model is suitable for forecasting the spatial distribution of short-term droughts for each season. In addition, ConvLSTM was evaluated for 1–10 days of lead time in 2018, and the results were averaged. We found that the model forecasting ability decreased as the lead time increased (Fig. S6), but the model performed well (high spatial correlation, $R^2 > 0.8$) for lead times of 1–5 days, indicating that the ConvLSTM model is well capable of short-term meteorological drought forecasting.

3.3. *Drought policy implications*

For areas where short-term droughts are frequent and of high intensity, we suggest that we should actively prepare for drought by, for

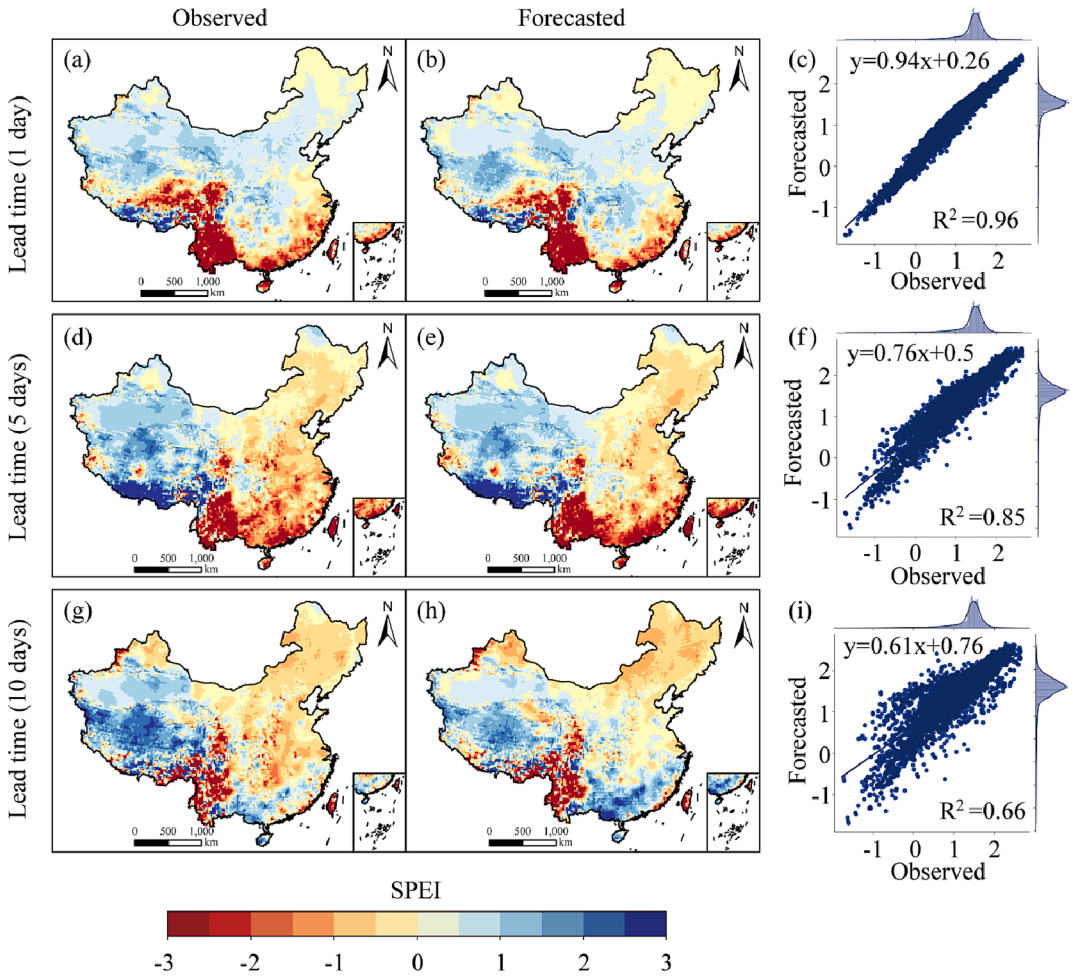

Fig. 10. The spatial forecast performance of the ConvLSTM model based on SPEI-5d for lead times of 1, 5, and 10 days.

example (1) improving water resource utilization efficiency and reducing waste through water-saving irrigation technology, water reuse, and soil moisture management; (2) building reservoirs and water conservancy projects in drought-prone areas to increase water storage and supply; (3) establishing a sound water resources management mechanism by strengthening water resources monitoring and early warning systems and taking timely countermeasures; and (4) improving the efficiency of agricultural production and reducing water resources consumption by selecting appropriate farming methods, crop planting structures, and irrigation methods. In addition, for long-term drought areas, options include (1) implementing regional water restriction measures to limit water consumption and reduce water waste; (2) optimizing water resources allocation by reallocating water resources from areas with abundant water to areas with water shortages to alleviate local drought conditions; and finally, (3) strengthening drought monitoring and early warning work by releasing drought warning information in a timely manner to guide people to take effective measures to reduce drought losses.

4. Conclusions

Meteorological drought is the antecedent of hydrological drought and agricultural drought, and the monitoring and forecasting of short-term meteorological drought can effectively avoid the damage caused by flash drought. We developed a pentad-scale (5-day) SPEI (SPEI-5d) to monitor and analyze the spatiotemporal distribution characteristics of short-term meteorological drought, and compared four time-series forecasting models (ARIMA, RF, RNN, and LSTM) and a spatiotemporal forecasting model (ConvLSTM) to fit and forecast SPEI-5d values in China. The conclusions are as follows:

(1) Short-term meteorological drought (SPEI-5d) was generally longer in northern China and shorter in southern China during 1962–2018. Most regions (61.9% of the area) showed a decreasing trend in drought severity, while about 69.6% of the area showed an increasing trend in drought intensity.
(2) The seasonal differences in the spatiotemporal distribution of short-term meteorological drought were large. In summer and autumn, the drought duration and severity were greatest in northwestern China. In spring and winter, the drought duration, severity, and intensity were greatest in southwestern China, but the drought intensity in southwestern China was weakest in summer and autumn.
(3) The performance of the ConvLSTM model in the test set was best among the models, and it was followed by LSTM, RNN, ARIMA, and finally the RF model. And there were seasonal differences in model performance, with generally higher accuracy in winter and lower in summer. The ConvLSTM model had the highest accuracy ($R^2 > 0.8$) for lead times of 1–5 days, indicating that the ConvLSTM model is suitable for short-term meteorological drought forecasting.

CRediT authorship contribution statement

Qi Zhang: Methodology, Formal analysis, Data curation, Visualization, Writing - original draft. **Chiyuan Miao:** Methodology, Formal

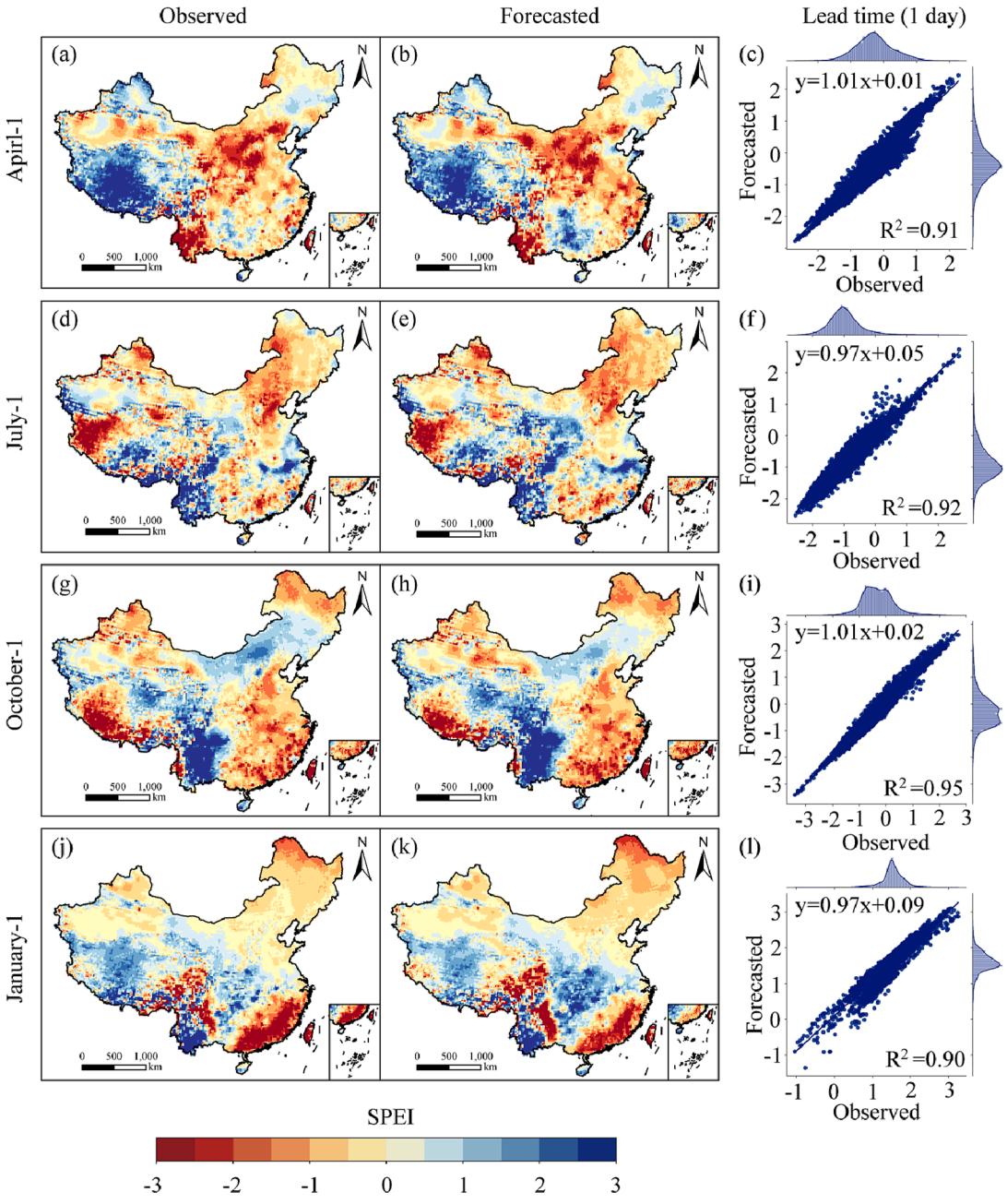

Fig. 11. The spatial forecast performance of the ConvLSTM model based on SPEI-5d for a lead time of 1 day for each season (we chose the first day of the middle month of each season in 2018).

analysis, Visualization, Supervision, Writing - original draft, Writing - review & editing. **Jiaojiao Gou:** Methodology, Formal analysis, Visualization, Writing - original draft, Writing - review & editing. **Haiyan Zheng:** Methodology, Writing - review & editing.

Declaration of Competing Interest

The authors declare that they have no known competing financial interests or personal relationships that could have appeared to influence the work reported in this paper.

Data availability

Data will be made available on request.

Acknowledgments

This work was supported by the National Natural Science Foundation of China (42041006), the Second Tibetan Plateau Scientific Expedition and Research Program (STEP) (No.2019QZKK0405) and the State Key Laboratory of Earth Surface Processes and Resource Ecology (2022-ZD-03).

Appendix A. Supplementary data

Supplementary data to this article can be found online at https://doi.org/10.1016/j.jhydrol.2023.129924.

References

Akbari Asanjan, A., Yang, T., Hsu, K., Sorooshian, S., Lin, J., Peng, Q., 2018. Short-term precipitation forecast based on the PERSIANN system and LSTM recurrent neural networks. J. Geophys. Res. Atmos. 123 (22) https://doi.org/10.1029/2018JD028375.

Alawsi, M.A., Zubaidi, S.L., Al-Bdairi, N.S.S., Al-Ansari, N., Hashim, K., 2022. Drought forecasting: A review and assessment of the hybrid techniques and data pre-processing. Hydrology 9 (7), 115. https://doi.org/10.3390/hydrology9070115.

Allen, R.G., Pereira, L.S., Raes, D., Smith, M., 1998. Crop evapotranspiration – Guidelines for computing crop water requirements - FAO Irrigation and drainage paper 56. Irrig. Drain. https://doi.org/10.1016/j.eja.2010.12.001.

Apurv, T., Xu, Y.-P., Wang, Z., Cai, X., 2019. Multidecadal changes in meteorological drought severity and their drivers in Mainland China. J. Geophys. Res. Atmos. 124 (23), 12937–12952.

Asgarimehr, M., Arnold, C., Weigel, T., Ruf, C., Wickert, J., 2022. GNSS reflectometry global ocean wind speed using deep learning: development and assessment of CyGNSSnet. Remote Sens. Environ. 269, 112801.

Belayneh, A., Adamowski, J., Khalil, B., Ozga-Zielinski, B., 2014. Long-term SPI drought forecasting in the Awash River Basin in Ethiopia using wavelet neural networks and wavelet support vector regression models. J. Hydrol. 508, 418–429. https://doi.org/10.1016/j.jhydrol.2013.10.052.

Bevacqua, A.G., Chaffe, P.L.B., Chagas, V.B.P., AghaKouchak, A., 2021. Spatial and temporal patterns of propagation from meteorological to hydrological droughts in Brazil. J. Hydrol. 603, 126902.

Buttafuoco, G., Caloiero, T., Coscarelli, R., 2015. Analyses of drought events in Calabria (Southern Italy) using standardized precipitation index. Water Resour. Manag. 29 (2), 557–573.

Chen, S., Hu, C., Barnes, B.B., Wanninkhof, R., Cai, W.-J., Barbero, L., Pierrot, D., 2019. A machine learning approach to estimate surface ocean pCO2 from satellite measurements. Remote Sens. Environ. 228, 203–226.

Chiang, F., Mazdiyasni, O., AghaKouchak, A., 2021. Evidence of anthropogenic impacts on global drought frequency, duration, and intensity. Nat. Commun. 12 (1) https://doi.org/10.1038/s41467-021-22314-w.

Christian, J.I., Basara, J.B., Hunt, E.D., Otkin, J.A., Furtado, J.C., Mishra, V., Xiao, X., Randall, R.M., 2021. Global distribution, trends, and drivers of flash drought occurrence. Nat. Commun. 12 (1) https://doi.org/10.1038/s41467-021-26692-z.

Cui, G., Ma, Q., Bales, R., 2022. Assessing multi-year-drought vulnerability in dense Mediterranean-climate forests using water-balance-based indicators. J. Hydrol. 606, 127431.

Dikshit, A., Pradhan, B., Alamri, A.M., 2021. Long lead time drought forecasting using lagged climate variables and a stacked long short-term memory model. Sci. Total Environ. 755, 142638 https://doi.org/10.1016/j.scitotenv.2020.142638.

Feng, P., Wang, B., Liu, D.L., Waters, C., Yu, Q., 2019. Incorporating machine learning with biophysical model can improve the evaluation of climate extremes impacts on wheat yield in south-eastern Australia. Agric. For. Meteorol. 275, 100–113.

Ford, T.W., Labosier, C.F., 2017. Meteorological conditions associated with the onset of flash drought in the Eastern United States. Agric. For. Meteorol. 247, 414–423.

Fundel, F., Jörg-Hess, S., Zappa, M., 2013. Monthly hydrometeorological ensemble prediction of streamflow droughts and corresponding drought indices. Hydrol. Earth Syst. Sci. 17 (1), 395–407.

Fung, K.F., Huang, Y.F., Koo, C.H., Soh, Y.W., 2020. Drought forecasting: A review of modelling approaches 2007–2017. J. Water Clim. Change 11 (3), 771–799. https://doi.org/10.2166/wcc.2019.236.

Gislason, P.O., Benediktsson, J.A., Sveinsson, J.R., 2006. Random Forests for land cover classification. Pattern Recogn. Lett. 27 (4), 294–300.

Gong, Z., Zhu, J., Li, T., Huang, D., Chen, X., Zhang, Q., 2022. The features of regional flash droughts in four typical areas over China and the possible mechanisms. Sci. Total Environ. 827, 154217.

Gou, Q., Zhu, Y., Lü, H., Horton, R., Yu, X., Zhang, H., Wang, X., Su, J., Liu, E., Ding, Z., Wang, Z., Yuan, F., 2022. Application of an improved spatio-temporal identification method of flash droughts. J. Hydrol. 604, 127224.

Ham, Y.-G., Kim, J.-H., Luo, J.-J., 2019. Deep learning for multi-year ENSO forecasts. Nature 573 (7775), 568–572.

Han, L., Zhang, Q., Zhang, Z., Jia, J., Wang, Y., Huang, T., Cheng, Y., 2021. Drought area, intensity and frequency changes in China under climate warming, 1961–2014. J. Arid Environ. 193, 104596.

Hao, Z., Hao, F., Singh, V.P., Xia, Y., Ouyang, W., Shen, X., 2016. A theoretical drought classification method for the multivariate drought index based on distribution properties of standardized drought indices. Adv. Water Resour. 92, 240–247.

Hao, Z., Singh, V.P., Xia, Y., 2018. Seasonal drought prediction: advances, challenges, and future prospects. Rev. Geophys. 56 (1), 108–141. https://doi.org/10.1002/2016RG000549.

Hosseini-Moghari, S.M., Araghinejad, S., 2015. Monthly and seasonal drought forecasting using statistical neural networks. Environ. Earth Sci. 74 (1), 397–412.

Jiao, W., Wang, L., Smith, W.K., Chang, Q., Wang, H., D'Odorico, P., 2021. Observed increasing water constraint on vegetation growth over the last three decades. Nat. Commun. 12 (1) https://doi.org/10.1038/s41467-021-24016-9.

Jong, B.-T., Newman, M., Hoell, A., 2022. Subseasonal meteorological drought development over the central United States during spring. J. Clim. 35 (8) https://doi.org/10.1175/jcli-d-21-0435.1.

Kim, S., Choi, C.-Y., Shahandashti, M., Ryu, K.R., 2022. Improving accuracy in predicting city-level construction cost indices by combining linear ARIMA and nonlinear ANNs. J. Manag. Eng. 38 (2) https://doi.org/10.1061/(asce)me.1943-5479.0001008.

Krizhevsky, A., Sutskever, I., Hinton, G.E., 2017. ImageNet classification with deep convolutional neural networks. Commun. ACM 60 (6), 84–90.

Le, J.A., El-Askary, H.M., Allali, M., Struppa, D.C., 2017. Application of recurrent neural networks for drought projections in California. Atmos. Res. 188, 100–106. https://doi.org/10.1016/j.atmosres.2017.01.002.

Lesk, C., Coffel, E., Winter, J., Ray, D., Zscheischler, J., Seneviratne, S.I., Horton, R., 2021. Stronger temperature–moisture couplings exacerbate the impact of climate warming on global crop yields. Nature Food 2 (9), 683–691. https://doi.org/10.1038/s43016-021-00341-6.

Li, X., Liang, S., Yuan, W., Yu, G., Cheng, X., Chen, Y., Zhao, T., Feng, J., Ma, Z., Ma, M., Liu, S., Chen, J., Shao, C., Li, S., Zhang, X., Zhang, Z., Sun, G.e., Chen, S., Ohta, T., Varlagin, A., Miyata, A., Takagi, K., Saiqusa, N., Kato, T., 2014. Estimation of evapotranspiration over the terrestrial ecosystems in China. Ecohydrology 7 (1), 139–149.

Li, L., She, D., Zheng, H., Lin, P., Yang, Z.-L., 2020. Elucidating diverse drought characteristics from two meteorological drought indices (SPI and SPEI) in China. J. Hydrometeorol. 21 (7), 1513–1530. https://doi.org/10.1175/jhm-d-19-0290.1.

Li, Q., Wang, Z., Shangguan, W., Li, L., Yao, Y., Yu, F., 2021. Improved daily SMAP satellite soil moisture prediction over China using deep learning model with transfer learning. J. Hydrol. 600, 126698.

Li, S., Yao, Z., Liu, Z., Wang, R., Liu, M., Adam, J.C., 2019. The spatio-temporal characteristics of drought across Tibet, China: derived from meteorological and agricultural drought indexes. Theor. Appl. Climatol. 137 (3–4), 2409–2424. https://doi.org/10.1007/s00704-018-2733-9.

Liang, M., Yuan, X., 2021. Critical role of soil moisture memory in predicting the 2012 Central United States flash drought. Front. Earth Sci. 9 https://doi.org/10.3389/feart.2021.615969.

Liu, J., Yuan, X., Zeng, J., Jiao, Y., Li, Y., Zhong, L., Yao, L., 2022. Ensemble streamflow forecasting over a cascade reservoir catchment with integrated hydrometeorological modeling and machine learning. Hydrol. Earth Syst. Sci. 26 (2), 265–278.

Ma, N., Szilagyi, J., Zhang, Y., Liu, W., 2019. Complementary-relationship-based modeling of terrestrial evapotranspiration across china during 1982–2012: validations and spatiotemporal analyses. J. Geophys. Res. Atmos. 124 (8), 4326–4351.

McKee, T. B., Nolan, J., Kleist, J., 1993. The relationship of drought frequency and duration to time scales. Preprints, Eighth Conf. on Applied Climatology, Amer. Meteor, Soc.

Miao, C.Y., Gou, J.J., Fu, B.J., Tang, Q.H., Duan, Q.Y., Chen, Z.S., Lei, H.M., Chen, J., Guo, J.L., Borthwich, A.G.L., Ding, W.F., Duan, X.W., Li, Y.G., Kong, D.X., Guo, X.Y., Wu, J.W., 2022. High-quality reconstruction of China's natural streamflow. Sci. Bull. 67 (5), 547–556. https://doi.org/10.1016/j.scib.2021.09.022.

Mishra, A.K., Singh, V.P., 2010. A review of drought concepts. J. Hydrol. 391 (1–2), 202–216. https://doi.org/10.1016/j.jhydrol.2010.07.012.

Mukherjee, S., Mishra, A.K., 2022. Global flash drought analysis: uncertainties from indicators and datasets. Earth's Future 10 (6). https://doi.org/10.1029/2022ef002660.

Oquab, M., Bottou, L., Laptev, I., Sivic, J., 2014. Learning and transferring mid-level image representations using convolutional neural networks. In Proceedings of the IEEE Computer Society Conference on Computer Vision and Pattern Recognition. 10.1109/CVPR.2014.222.

Otkin, J.A., Svoboda, M., Hunt, E.D., Ford, T.W., Anderson, M.C., Hain, C., Basara, J.B., 2018. Flash droughts: A review and assessment of the challenges imposed by rapid-onset droughts in the United States. Bull. Am. Meteorol. Soc. 99 (5), 911–919. https://doi.org/10.1175/BAMS-D-17-0149.1.

Paprotny, D., Sebastian, A., Morales-Nápoles, O., Jonkman, S.N., 2018. Trends in flood losses in Europe over the past 150 years. Nat. Commun. 9 (1) https://doi.org/10.1038/s41467-018-04253-1.

Park, S., Im, J., Han, D., Rhee, J., 2020. Short-term forecasting of satellite-based drought indices using their temporal patterns and numerical model output. Remote Sens. (Basel) 12 (21), 1–21. https://doi.org/10.3390/rs12213499.

Potop, V., Boroneanţ, C., Možný, M., Štěpánek, P., Skalák, P., 2014. Observed spatiotemporal characteristics of drought on various time scales over the Czech Republic. Theor. Appl. Climatol. 115 (3-4), 563–581.

Qing, Y., Wang, S., Ancell, B.C., Yang, Z.L., 2022. Accelerating flash droughts induced by the joint influence of soil moisture depletion and atmospheric aridity. Nat. Commun. 13 (1) https://doi.org/10.1038/s41467-022-28752-4.

Reichstein, M., Camps-Valls, G., Stevens, B., Jung, M., Denzler, J., Carvalhais, N., Prabhat., 2019. Deep learning and process understanding for data-driven Earth system science. Nature 566 (7743). https://doi.org/10.1038/s41586-019-0912-1.

Retsch, M.H., Jakob, C., Singh, M.S., 2022. Identifying relations between deep convection and the large-scale atmosphere using explainable artificial intelligence. J. Geophys. Res. Atmos. 127 (3) https://doi.org/10.1029/2021JD035388.

Schreiner-McGraw, A.P., Ajami, H., 2021. Delayed response of groundwater to multi-year meteorological droughts in the absence of anthropogenic management. J. Hydrol. 603, 126917 https://doi.org/10.1016/j.jhydrol.2021.126917.

Shen, H., Li, T., Yuan, Q., Zhang, L., 2018. Estimating regional ground-level PM 2.5 directly from satellite top-of-atmosphere reflectance using deep belief networks. J. Geophys. Res. Atmos. 123 (24) https://doi.org/10.1029/2018JD028759.

Shi, X., Chen, Z., Wang, H., Yeung, D.Y., Wong, W.K., Woo, W.C., 2015. Convolutional LSTM network: A machine learning approach for precipitation nowcasting. Adv. Neural Inf. Process. Syst., 2015-Janua, 802–810.

Stagge, J.H., Tallaksen, L.M., Gudmundsson, L., van Loon, A.F., Stahl, K., 2015. Candidate distributions for climatological drought indices (SPI and SPEI). Int. J. Climatol. 35 (13) https://doi.org/10.1002/joc.4267.

Su, B., Huang, J., Fischer, T., Wang, Y., Kundzewicz, Z.W., Zhai, J., et al., 2018. Drought losses in China might double between the 1.5 °C and 2.0 °C warming. Proc. Natl. Acad. Sci. U.S.A. 10.1073/pnas.1802129115.

Sun, L., Mitchell, S.W., Davidson, A., 2012. Multiple drought indices for agricultural drought risk assessment on the Canadian prairies. Int. J. Climatol. 32 (11), 1628–1639.
Tan, H., Cai, R., Chen, J., Huang, R., 2017. Decadal winter drought in Southwest China since the late 1990s and its atmospheric teleconnection. Int. J. Climatol. 37 (1), 455–467.
Taylor, K.E., 2001. Summarizing multiple aspects of model performance in a single diagram. J. Geophys. Res. Atmos. 106 (D7), 7183–7192.
Thirumalai, K., DInezio, P.N., Okumura, Y., Deser, C., 2017. Extreme temperatures in Southeast Asia caused by El Nin? And worsened by global warming. Nat. Commun. 8 https://doi.org/10.1038/ncomms15531.
Tian, W., Wu, J., Cui, H., Hu, T., 2021. Drought prediction based on feature-based transfer learning and time series imaging. IEEE Access 9, 101454–101468.
Ulloa, N.I., Yun, S.H., Chiang, S.H., Furuta, R., 2022. Sentinel-1 spatiotemporal simulation using convolutional LSTM for flood mapping. Remote Sens. (Basel) 14 (2). https://doi.org/10.3390/rs14020246.
Vicente-Serrano, S.M., Beguería, S., López-Moreno, J.I., 2010. A multiscalar drought index sensitive to global warming: The standardized precipitation evapotranspiration index. J. Clim. 23 (7), 1696–1718. https://doi.org/10.1175/2009JCLI2909.1.
Wang, X., 2022. Research on the prediction of per capita coal consumption based on the ARIMA–BP combined model. Energy Rep. 8, 285–294.
Wang, W., Mao, W., Tong, X., Xu, G., 2021b. A novel recursive model based on a convolutional long short-term memory neural network for air pollution prediction. Remote Sens. (Basel) 13 (7). https://doi.org/10.3390/rs13071284.
Wang, Y., Yuan, X., 2021. Anthropogenic speeding up of south china flash droughts as exemplified by the 2019 summer-autumn transition season. Geophys. Res. Lett. 48 (9) https://doi.org/10.1029/2020GL091901.
Wang, Q., Zeng, J., Qi, J., Zhang, X., Zeng, Y., Shui, W., Xu, Z., Zhang, R., Wu, X., Cong, J., 2021a. A multi-scale daily SPEI dataset for drought characterization at observation stations over mainland China from 1961 to 2018. Earth Syst. Sci. Data 13 (2), 331–341.
Warter, M.M., Singer, M.B., Cuthbert, M.O., Roberts, D., Caylor, K.K., Sabathier, R., Stella, J., 2021. Drought onset and propagation into soil moisture and grassland vegetation responses during the 2012–2019 major drought in Southern California. Hydrol. Earth Syst. Sci. 25 (6), 3713–3729. https://doi.org/10.5194/hess-25-3713-2021.
Wu, J., Chen, X., 2019. Spatiotemporal trends of dryness/wetness duration and severity: the respective contribution of precipitation and temperature. Atmos. Res. 216, 176–185. https://doi.org/10.1016/j.atmosres.2018.10.005.
Wu, J., Miao, C., Zheng, H., Duan, Q., Lei, X., Li, H., 2018. Meteorological and hydrological drought on the loess Plateau, China: evolutionary characteristics, impact, and propagation. J. Geophys. Res. Atmos. 123 (20), 11569–11584. https://doi.org/10.1029/2018JD029145.
Xu, H.-J., Wang, X.-P., Zhao, C.-Y., Shan, S.-Y., Guo, J., 2021c. Seasonal and aridity influences on the relationships between drought indices and hydrological variables over China. Weather Clim. Extremes 34, 100393.
Xu, D., Zhang, Q.i., Ding, Y., Huang, H., 2020. Application of a hybrid ARIMA-SVR model based on the SPI for the forecast of drought—A case study in Henan Province, China. J. Appl. Meteorol. Climatol. 59 (7), 1239–1259.
Xu, Y., Zhang, X., Hao, Z., Hao, F., Li, C., 2021a. Projections of future meteorological droughts in China under CMIP6 from a three-dimensional perspective. Agric. Water Manag. 252, 106849.
Xu, D., Zhang, Q., Ding, Y., Zhang, D., 2021b. Spatiotemporal pattern mining of drought in the last 40 years in china based on the spei and space–time cube. J. Appl. Meteorol. Climatol. 60 (9), 1219–1230. https://doi.org/10.1175/JAMC-D-21-0049.1.
Xu, D., Zhang, Q., Ding, Y., Zhang, D., 2022. Application of a hybrid ARIMA-LSTM model based on the SPEI for drought forecasting. Environ. Sci. Pollut. Res. 29 (3), 4128–4144. https://doi.org/10.1007/s11356-021-15325-z.
Yang, P., Wang, N., Zhao, L., Su, B., Niu, Z., Zhao, H., 2022. Responses of grassland ecosystem carbon fluxes to precipitation and their environmental factors in the Badain Jaran Desert. Environ. Sci. Pollut. Res. 29 (50), 75805–75821.
Yang, S., Yang, D., Chen, J., Zhao, B., 2019. Real-time reservoir operation using recurrent neural networks and inflow forecast from a distributed hydrological model. J. Hydrol. 579, 124229.
Yu, M., Li, Q., Hayes, M.J., Svoboda, M.D., Heim, R.R., 2014. Are droughts becoming more frequent or severe in China based on the standardized precipitation evapotranspiration index: 1951–2010? Int. J. Climatol. 34 (3), 545–558. https://doi.org/10.1002/joc.3701.
Yuan, X., Zhang, M., Wang, L., Zhou, T., 2017. Understanding and seasonal forecasting of hydrological drought in the Anthropocene. Hydrol. Earth Syst. Sci. 21 (11), 5477–5492.
Yuan, X., Wang, L., Wu, P., Ji, P., Sheffield, J., Zhang, M., 2019. Anthropogenic shift towards higher risk of flash drought over China. Nat. Commun. 10 (1) https://doi.org/10.1038/s41467-019-12692-7.
Zhang, Q., Miao, C., Gou, J., Wu, J., Jiao, W., Song, Y., Xu, D., 2022a. Spatiotemporal characteristics of meteorological to hydrological drought propagation under natural conditions in China. Weather Clim. Extremes 38, 100505.
Zhang, J., Sun, F., Xu, J., Chen, Y., Sang, Y.F., Liu, C., 2016. Dependence of trends in and sensitivity of drought over China (1961–2013) on potential evaporation model. Geophys. Res. Lett. 43 (1), 206–213. https://doi.org/10.1002/2015GL067473.
Zhang, J.J.Y., Sun, L., Rainham, D., Dummer, T.J.B., Wheeler, A.J., Anastasopolos, A., Gibson, M., Johnson, M., 2022b. Predicting intraurban airborne PM1.0-trace elements in a port city: Land use regression by ordinary least squares and a machine learning algorithm. Sci. Total Environ. 806, 150149.
Zhang, Y., You, Q., Mao, G., Chen, C., Li, X., Yu, J., 2021. Flash drought characteristics by different severities in humid subtropical basins: A case study in the Gan River Basin, China. J. Clim. 34 (18) https://doi.org/10.1175/JCLI-D-20-0596.1.
Zhao, W. (2020). Extreme weather and climate events in China under changing climate. Natl. Sci. Rev. 10.1093/nsr/nwaa069.
Zheng, H., Miao, C., Li, X., Kong, D., Gou, J., Wu, J., Zhang, S., 2022. Effects of vegetation changes and multiple environmental factors on evapotranspiration across china over the past 34 years. Earth's Future 10 (4). https://doi.org/10.1029/2021EF002564.